



IAFSS 12th Symposium 2017

## An integrated approach for tactical monitoring and data-driven spread forecasting of wildfires



Mario M. Valero, Oriol Rios, Christian Mata, Elsa Pastor, Eulàlia Planas\*

Center for Technological Risk Studies, Universitat Politècnica de Catalunya - BarcelonaTech. c/ Eduard Maristany, 10-14 (EEBE), 08019 Barcelona, Spain

### ARTICLE INFO

#### Keywords:

Forest fires  
Remote sensing  
Thermal infrared  
Unmanned aerial vehicles  
Data assimilation  
Fire behaviour  
Modelling  
Forecast

### ABSTRACT

In recent times there have been increasing efforts to integrate technology into wildfire management, especially in the fields of tactical monitoring and simulation. On the one hand, thermal infrared imaging (TIR) systems have been installed aboard surveillance aircraft including unmanned systems (UAS). On the other, there exists a variety of models and simulators able to forecast the fire spread. However, both fields currently present significant limitations. While relevant information is still extracted manually from aerial thermal imagery and is most times merely qualitative, simulators' accuracy on fire spread prediction has proved insufficient. To solve these issues, this article presents a twofold methodology to couple meaningful automated wildfire monitoring with accurate fire spread forecasting. The main goals are to, firstly, automatically process aerial TIR imagery so that valuable information can be produced in real time during the event and, secondly, use this information to adjust a Rothermel-based simulator in order to improve its accuracy on-line. The fire perimeter location is tracked automatically through an unsupervised edge detector. Afterwards, an assimilation module uses the remotely sensed data to optimise the simulator's fuel and wind parameters, which are assumed to remain constant for a certain period of time. Subsequently, the optimum parameters' values are used to issue a fire evolution forecast. All outputs are projected onto the corresponding Digital Terrain Model (DTM) and integrated into a Geographic Information System (GIS) for visualization. The global system was validated using two large-scale experiments. If these algorithms can be applied to a sufficiently rich and varied set of experimental data and further developed to cope with more complex scenarios, they could eventually be incorporated into a fire management decision support system.

### 1. Introduction

Forest fires have been gaining attention in recent times. Partially favoured by global warming, the annual number of fires and the subsequent burned area have been increasing during the past decades [1,2] in the European Mediterranean region, and have been predicted to continue rising in the near future [3,4]. Furthermore, phenomena such as eruptive fires or fire whirls appear more and more frequently and worsen the fact that wildfire dynamics are not yet completely well understood [5,6]. In extreme cases, a significant amount of casualties occur as a consequence of unforeseen fire evolution, e.g. in Australia's Black Saturday in 2009 (173 victims) or in Yarnell Hill, Arizona, US, in 2013 (19 victims). Even when there are no casualties, important economic losses are suffered and large budgets spent [7].

Motivated by these reasons, there have been important technological advancements related to fire management. Remote Sensing systems have been developed and installed aboard a variety of platforms [8]. Spaceborne imagery, although currently used for tasks such

the estimation of surface fuel loading, hot-spot detection and remote measurement of burned areas, presents too coarse spatial and temporal resolutions to be suitable for active fire surveillance. On the contrary, airborne thermal infrared imagers proved very promising and are currently operative in several cases [9–12]. However, fire properties are not yet extracted automatically. So far, images are in general analysed qualitatively and fire front locations, when computed, are delineated manually [13–16]. On the other hand, there exist a number of mathematical, physical and semi-empirical models for wildfire propagation simulation [17–20]. However, no solution has been found suitable for implementation during the incident management as part of a decision support system (DDS). High-accuracy simulators based on computational fluid dynamics (CFD) [21–24] require enormous computational resources and their use is thus restricted to research studies and reduced simulation domains [25], whereas models which could be run in an operational time-constrained framework [26,27] have proved unable to successfully predict the observed rates of spread (ROS) [28]. Moreover, a problem common to both types of simulators is the

\* Corresponding author.

Nomenclature		Greek	
$A$	Area within the fire perimeter	$\alpha$	Terrain aspect (rad)
$c$	Set of Canny's hysteresis thresholds candidates	$\delta$	Fuel depth (m)
$M_f$	Fuel moisture content (%)	$\varphi$	Terrain slope (rad)
$M_x$	Fuel moisture of extinction (%)	$\sigma$	Gaussian filter standard deviation
ROS	Rate of Spread (m/min)	$\theta$	Wind direction at mid-flame height (rad)
SAV	Fuel surface area-to-volume ratio ( $m^{-1}$ )	Superscripts	
$U$	Wind speed at mid-flame height (m/s)	$ob$	observed
$W_o$	Fuel oven-dry fuel loading ( $kg/m^2$ )	$m$	modelled

scarcity of precise data available to initialise them [6]. Data assimilation was adopted as an alternative to make use of the advantageous speed of simpler methods while improving their accuracy [29–36]. Its rationale is based on the assimilation of the observed fire perimeter

location at different times (also called isochrones) and the subsequent optimisation of fuel and weather parameters so that modelled fire evolution resembles the observed. In this context, we developed an integrated system built upon

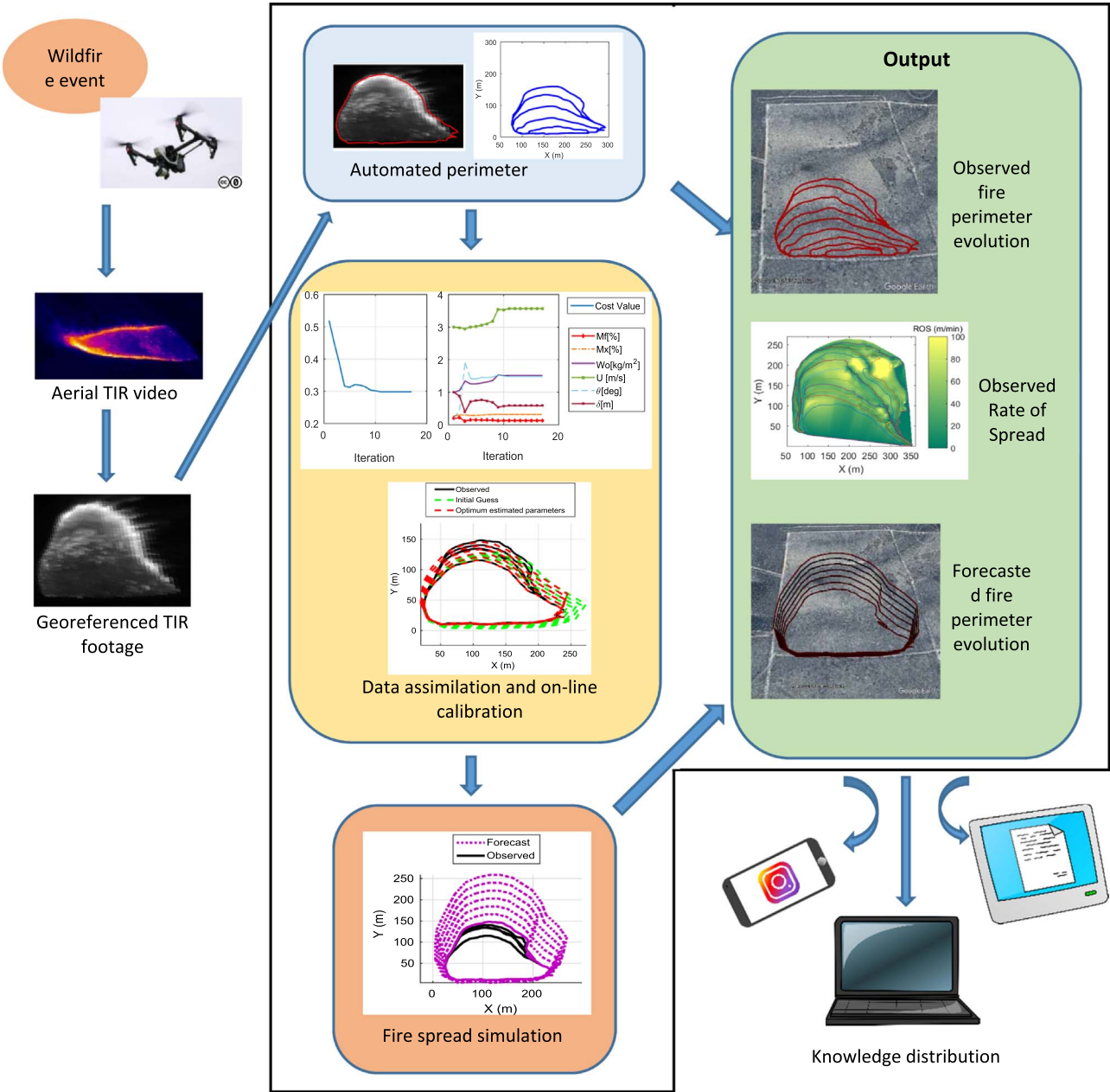


Fig. 1. Block diagram of the presented system. The tasks inside the box fall within the scope of this article.

previous works conducted along these two lines. The fire spread simulator published in [35,36] was further developed so that it could manage fuel properties independently and cope with digital elevation maps, therefore handling more general scenarios. Moreover, the observed isochrones needed for calibration, which had been provided manually, can now be detected automatically using thermal aerial infrared (TIR) imaging and the algorithms presented in [37,38]. The following study suggests that the coupling of these methodologies

extends the applicability of the independent algorithms and helps to solve some of their issues. Hereafter we present a system which, given a TIR georeferenced footage that shows the fire development, can emit, automatically and in real time, a reliable forecast of the next minutes' fire evolution. The fact of using TIR imagery as the only source of optical data reduces the system complexity, weight and cost in comparison with hyperspectral imagers. The rest of the paper is organised as follows: Section 2 gives a general overview of the system.

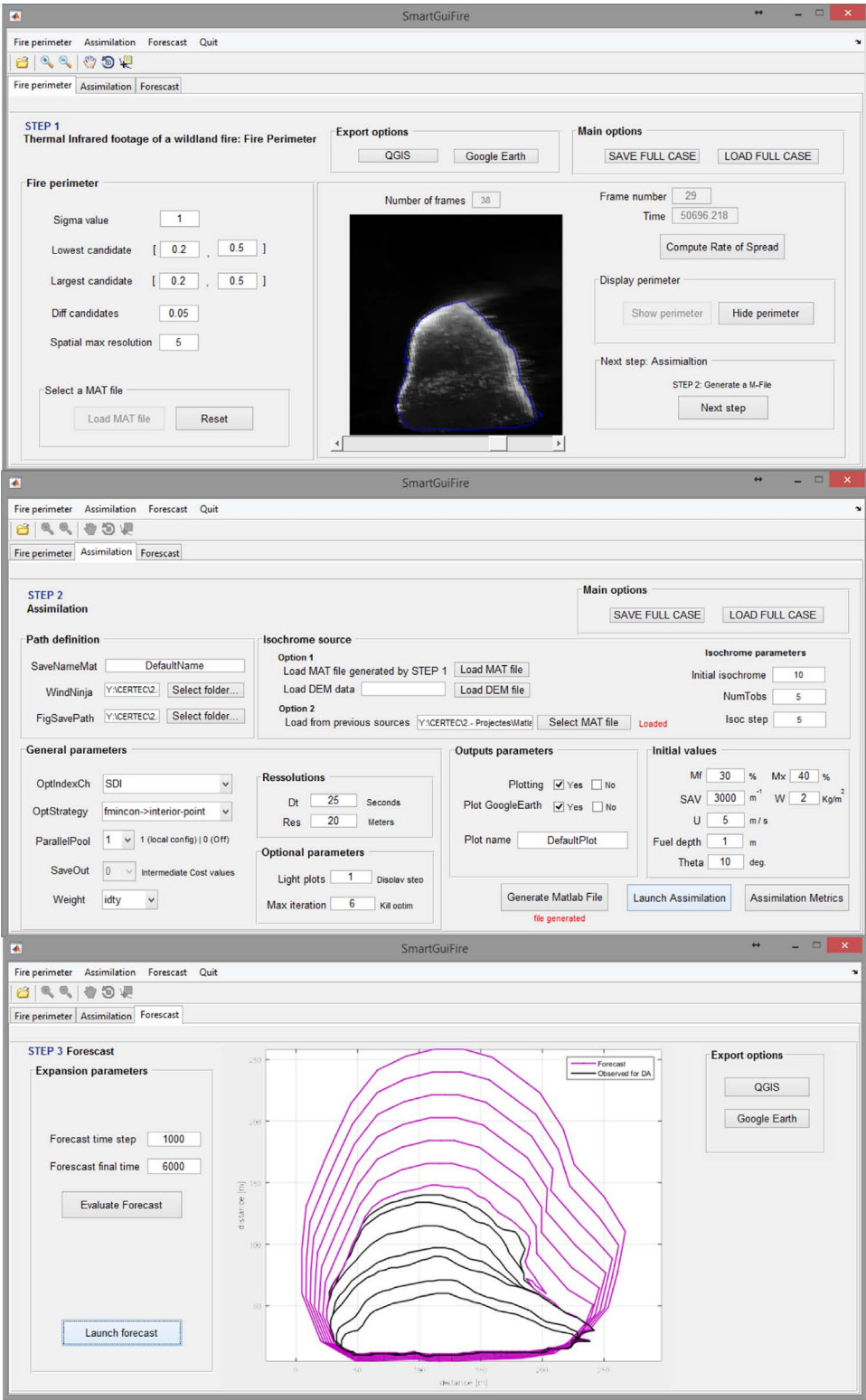


Fig. 2. Screenshots of the system's graphical user interface.

Section 3 describes the different implemented algorithms. Section 4 presents the data used for validation and Section 5 shows the results of such validation. Finally, concluding remarks and suggestions for future work are included in Section 6.

## 2. System overview

Fig. 1 shows the block diagram of the system. Inside the box are the tasks included and analysed in this article. It is important to remark that the communications infrastructure needed to centralise remote sensed data and distribute generated knowledge falls beyond the scope of this publication. Fig. 2 displays sample screenshots of the graphical user interface. This interface is composed of three tabs dedicated to the three different tasks performed by the algorithm, which are described in Sections 3.1, 3.2 and 3.3. Although intimately related, these three tasks may be performed independently if desired. The “Assimilation” tab, for instance, may use the fire perimeter evolution provided by the “Fire perimeter” tab but could as well operate with externally loaded isochrones. Similarly, observed fire perimeter evolution or ROS fields may be computed once and saved for future analysis. All needed inputs and parameters can be directly introduced, loaded from a configuration file or set to default values. Output is displayed in the same window and may be navigated for assessment. Finally, generated geographical information is output in formats compatible with QGIS (vector layers) and GoogleEarth (.kml files).

## 3. Methodology

### 3.1. Automated perimeter tracking

The studies presented in [37,38] showed how edge detection algorithms can be applied to aerial thermal imagery to locate the burning interface of a wildland fire more meaningfully and robustly than simply using intensity thresholding techniques. After testing several edge detectors, the Canny method [39] was recommended since it produced the most accurate and smooth fire fronts. Following this advice, the Canny method was taken as the core of our algorithm and was complemented with the necessary pre- and post-processing modules. The core edge detector is based on the double thresholding of the intensity gradient magnitude and incorporates connectivity analysis in order to include in its output points which present low gradient values (weak edges) but are highly connected with points with high gradient values (strong edges).

The most important part of the pre-processing is the optimisation of the edge detector input parameters. In order to work properly, the Canny method needs 3 parameters to be correctly defined: the standard deviation of the Gaussian filter applied for initial noise reduction plus two hysteresis thresholds. The first is given a constant value for all study cases, whereas the two thresholds are automatically estimated on-line for each frame using the methodology presented in [40]. This methodology uses only the information present in the image to select the best hysteresis thresholds for the Canny detector from a given set of candidates, which is as well kept constant. Assigned values are shown in Table 1.

Several post-processing steps are also needed after applying the edge detector. Firstly, the detected edge is thinned and its points are ordered in either clockwise or counter-clockwise direction. Secondly, different lines assumed to belong to the same edge are connected with each other so that gaps are removed. Afterwards, the burned perimeter is updated by adding the latest detected fire advance. Finally, lines representing fire perimeters are reduced to the minimum amount of points needed to meet the defined resolution requirements. This helps to speed-up further computations and limit the appearance of topological problems during the simulation stage. The spatial resolution of fire perimeters is at all times kept between 5 and 10 m for the study cases presented here, although these values can be modified if needed.

Once the geographic position of the fire perimeter is known at each time, it is imported to QGIS, an open-source geographic information system which allows the easy development of Python plug-ins. These results can be superimposed to relevant topographic maps and digital elevation models, thus enhancing the utility of the produced information. Furthermore, when a sufficient number of isochrones (i.e. fire perimeter positions) are available, they are used to extract data about the observed fire behaviour (yellow box in Fig. 1), which is afterwards input to the simulating module (orange box in Fig. 1).

### 3.2. Front spread simulation

The fire spread is simulated following the approach detailed in [35,36]. The fire front rate of spread is estimated using Rothermel's model [41] and the front is propagated through Huygens' elliptical expansion [42]. Rothermel's surface fire spread model uses a source-sink energy balance to relate the fire-line rate of spread (ROS) with relevant fuel, wind and terrain parameters. Through empirical correlations, the ROS can finally be expressed as a function of the fuel depth ( $\delta$ ), the oven-dry fuel loading ( $W_o$ ), the surface area-to-volume ratio (SAV), the fuel moisture content ( $M_f$ ), the moisture of extinction ( $M_x$ ), the wind mid-flame speed ( $U$ ), the wind main direction ( $\theta$ ) and the terrain slope ( $\varphi$ ) and aspect ( $\alpha$ ), as shown in Eq. (1).

$$ROS = F(\delta, W_o, SAV, M_f, M_x, U, \theta, \varphi, \alpha) \quad (1)$$

The current version of the algorithm introduces significant changes in the way the simulator manages fuel properties. The methodology presented in [36] took advantage of a linear relationship detected between ROS and  $\delta$  to compact all fuel-related parameters into two global variables:  $\delta$  and  $I_{mfw}$ . However, this assumption limited the fire dynamics' description and the knowledge which could be assimilated. Conversely, the algorithm proposed here can handle all fuel parameters independently. Furthermore, terrain is no longer assumed to be flat and elevation, aspect and slope are introduced into the analysis if an appropriate digital elevation model is available.

The fire perimeter continues to be propagated using Huygens' elliptical expansion accompanied by the point management modules needed to solve topological problems inherent to its Lagrangian formulation. Loops evolved from convex regions are filtered and points conforming the perimeter are re-distributed so that sharp zones present enough resolution while the amount of nodes in smooth areas is reduced to an optimum value [36].

### 3.3. Data assimilation and on-line calibration

The front spread simulator needs 9 parameters in total in order to estimate the rate of spread (see Eq. (1)), from which 5 correspond to fuel properties, 2 to wind conditions and the remaining 2 to terrain characteristics. The tremendous uncertainty about these data is one of the main reasons why wildland fire simulators are usually unable to reproduce actual fire evolution. Precise information about some fuel properties such as the oven-dry fuel loading, the surface to volume ratio or the moisture content is almost impossible to obtain except through intense field surveys combined with specific laboratory tests. Furthermore, their values can vary substantially over wide areas. Similarly, wind speed and direction at mid-flame height is barely

**Table 1**  
Fixed input parameters for the unsupervised edge detection algorithm (taken from [38]).

Parameter	Value
Gaussian filter standard deviation ( $\sigma$ )	4
Hysteresis threshold candidates	$c = \{(c1, c2)   c1 < c2\}$ such that $c1 \in [0.2, 0.7] \wedge (\exists k \in \mathbb{Z}) (c1 = 0.05 \cdot k)$ $c2 \in [0.5, 0.9] \wedge (\exists k \in \mathbb{Z}) (c2 = 0.05 \cdot k)$



deducible from 10 m-height measurements. Terrain characteristics, on the contrary, are usually accessible through public available maps. If the fire can be precisely located, local slope and aspect values can be computed from digital elevation models.

Therefore, the global system, after locating the perimeter, consults the loaded DEM and reads the slope and aspect angles at each required position. These data are subsequently input to the simulator. On the contrary, the first 7 parameters are considered unknown a-priori due to the usual scarcity of available data about fuel properties and local mid-flame wind values, and must be estimated through a data-assimilation-based optimisation process. The assimilation strategy is based on an algorithm developed by Byrd et al. [43] which uses sequential quadratic programming techniques. Since all parameters correspond to actual physical properties, their values are constrained to known validity ranges. Furthermore, two of them, namely the fuel moisture content ( $M_f$ ) and the moisture of extinction ( $M_x$ ) are related to each other and must at all times satisfy the additional inequality bound  $M_f < M_x$ . Within these validity ranges parameters are allowed to vary until the optimum combination is found. The space search is performed by a non-linear optimisation algorithm that can switch between a line search method and a trust region iteration which guarantees progress towards a relative minimum [44]. If an iteration tries to assign to any parameter a value outside its validity range, this parameter is reset to the previous estimated value. Convergence is assumed to be achieved when all parameters, as well as the cost function, vary less than a given threshold in two consecutive iterations.

The cost function is a key aspect in any optimisation problem. In this case, the cost function must measure the similarity between the observed and modelled perimeters, and is to be reduced until a minimum is found. As discussed in [36,45], no index seems to have stood out from the many existing options when it comes to compare fire perimeter shapes. Therefore, our system is versatile and can use different similarity indices to define the cost function. Table 2 summarises a few already implemented, which are based on standard metrics. Nonetheless, any other index which decreases when two perimeters' shapes approach to each other may be implemented.

Whichever index is selected, it is computed over a set of pairs of isochrones and all values are added up, with the possibility of including some weighting distribution in order to give more importance to the most recent data:

$$\text{Cost value} = \sum_{i=1}^{i=N_d} W_i \cdot \text{Index}_i \quad (2)$$

where *Index* might be any of the indices in Table 2,  $W_i$  are weighting coefficients and  $N_d$  is the total number of assimilated isochrones. In the present study,  $W_i = 1$  was taken for all  $i$ . Sorensen's index was used to compute the cost function since the SDI index is not constrained and Jaccard's is in general more importantly affected by variations in the fire size.

#### 4. Validation data

The presented methodology was applied for assessment to two scenarios, hereafter named A and B. Both correspond to field experimental burns conducted in horizontal plots of 9 ha and 25 ha respectively, fuel being mallee-heath shrubs [49,50]. These experiments were recorded using visible and thermal infrared cameras manually operated by the crew aboard a surveillance helicopter (see sample frames in Fig. 3). Notice how the presence of heavy smoke makes visible footages virtually useless. Thermal images were acquired with a FLIR AGEMA Thermovision 570-Pro camera equipped with a spectral range of 7.5–13  $\mu\text{m}$ , a temporal resolution of 5 frames per second and a spatial resolution of 240×320 pixels. Owing to the difference in plot size and distance between the fire and the camera, pixels were projected to the ground with different sizes in each

scenario. The real length of pixels' sides is approximately 1 m for scenario A and 3 m for scenario B. The employed footages have a duration of 360 s and 220 s, respectively. The footage in scenario A commenced shortly after ignition whereas the footage in scenario B was started during the fire development.

Due to the lack of geo-positional (GPS) and inertial (IMU) data, a subset of frames from both TIR footages were manually geo-referenced using ground control points (GCP) and a direct linear transformation algorithm (DLT) [51]. This subset was obtained by selecting one frame every 10 s in each footage and constituted the input data for the following study. In scenario A, 80 s after ignition were discarded. The total amount of finally available georeferenced frames was 28 for scenario A and 21 for scenario B. Fire perimeters were delineated manually and taken as reference for the algorithm's assessment. Fig. 4 shows the two resulting subsets of reference isochrones.

#### 5. Validation results

The ability of the system to locate the fire perimeter was assessed for the whole duration of both footages through comparison with the reference isochrones. Qualitative results are displayed in Fig. 5, where some isochrones have been removed for clarity's sake. Automatically detected perimeters were also evaluated quantitatively using the similarity indices exposed in Table 2, as shown in Fig. 6. These indices move towards zero when the two perimeters being compared approach each other, i.e. lower index values mean better results. In general, agreement is considered satisfactory when index values stay below 0.1.

Figs. 5 and 6 show an overall adequate agreement between automatic and manual perimeters in scenario A as all indices lay under 0.1 for most of the frames. Higher values observed in the first frames of scenario A appeared as a consequence of the reduced fire size during the initial period, since the reference fire area is present in the denominator of all indices' expressions. Similarly, although results for scenario B may seem of lower quality at first, a more detailed look at problematic frames proved most errors were not directly derived from a poor performance of the algorithm. The system was able to track the fire front and adequately reproduced the fire growth. However, it was not initiated at the same time the fire started but some minutes after ignition, and therefore it was unable to capture the initial fire shape. This initial error was subsequently maintained during the rest of the footage. As exemplified in Fig. 7, the largest contribution to the measured errors in the scenario B came from the back of the fire, not from the fire front.

However, there is an issue the fire tracker could not solve successfully: the presence of flames. Flames flicker and rise from the ground and, despite being part of the fire perimeter, are to be avoided when the latter's actual position is to be detected. Although the tracking method implemented in our system is not affected by flames when these have a reduced size, the methodology used to georeference the original

**Table 2**

Implemented indices to measure perimeter similarity during the optimisation algorithm. A is the area enclosed by the fire perimeter, <sup>ob</sup> means observed and <sup>m</sup> stands for modelled.

Standard similarity metrics	
Absolute areal error	$A^{ob} \oplus A^m$
Shape deviation index (SDI) [46]	$\frac{A^{ob} \oplus A^m}{A^{ob}}$
Sorensen's index <sup>a</sup> [47]	$2 \cdot \frac{A^{ob} \cap A^m}{A^{ob} + A^m}$
Jaccard's index <sup>a</sup> [48]	$\frac{A^{ob} \cap A^m}{A^{ob} \cup A^m}$

<sup>a</sup> Original Sorensen's and Jaccard's indices approach 1 when similarity increases. Therefore, they were subtracted to 1 in this implementation as the cost function is to decrease when similarity increases.



**Fig. 3.** Sample TIR (left) and visible (right) frames of the experimental footages used for validation. Top: scenario A. Bottom: scenario B.

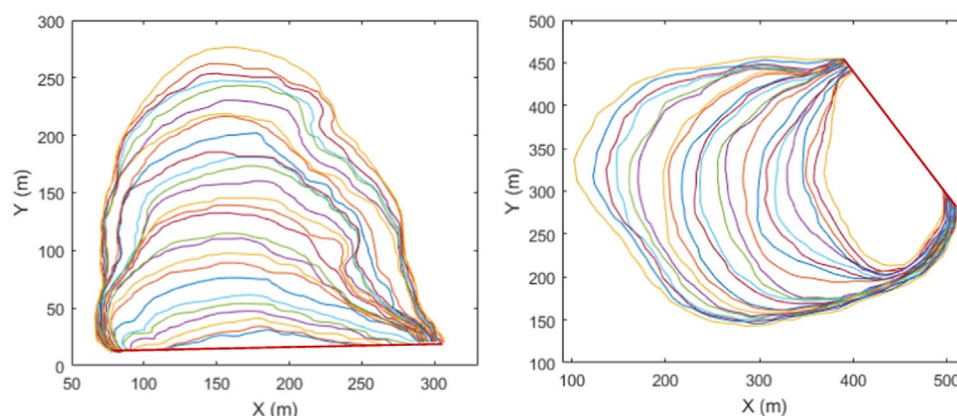


**Fig. 4.** Reference isochrones, obtained manually every 10 s for each validation scenario. Left: scenario A; time window 80–360 s. Right: scenario B; time window 10–220 s. Time origin represents footage start and does not coincide with ignition.

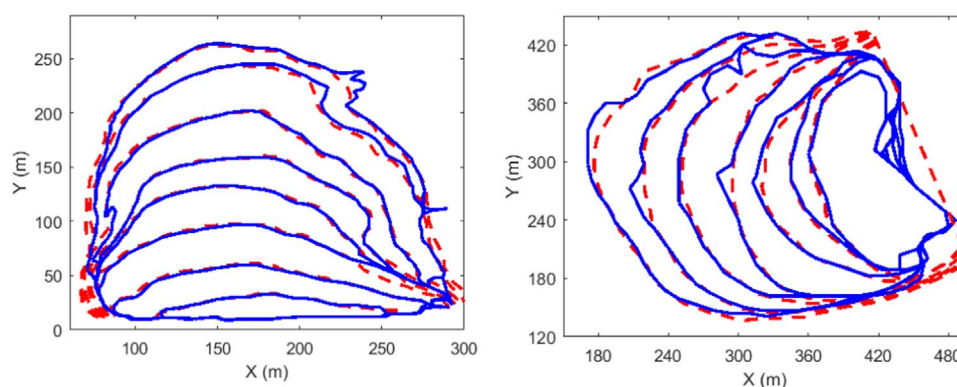


**Fig. 5.** Results of the perimeter tracking module (blue solid lines) qualitatively compared to the reference perimeters (red dashed lines). Left: Scenario A; isochrones in the time window 80–360 s, plotted every 40 s. Right: scenario B; isochrones in the time window 240–440 s, plotted every 40 s. (For interpretation of the references to color in this figure legend, the reader is referred to the web version of this article.)

footages makes flames appear larger in the georeferenced footage than they actually are. Georeferencing was performed through a 2D projective transformation which map points from the camera plane onto the ground plane. A consequence of this algorithm being 2-dimensional is that every object standing out of any of these planes is bound to be distorted through the projection. This is the case of flames, which stand vertically out of the ground plane. See Fig. 8 for examples.

The performance of the complete system was assessed by performing one tracking-assimilation-forecast sequence for each footage simulating operational conditions. The perimeter tracking module was

assumed to be active since the beginning of the footage in both cases. At some point ( $t_0$ ), a forecast was required. The forecast demand was placed at 230 s in scenario A and at 140 s in scenario B, which approximately corresponds to the middle time of both footages. The user was able to select how many isochrones must be assimilated as well as the separation between them. In this case, 5 isochrones were assimilated in both scenarios, at 10-s intervals in scenario A and at 20-s intervals in scenario B. This distinction was made based on the different scales of both experiments. Fire B was considerably larger and prolonged than fire A. Consequently, larger assimilation windows

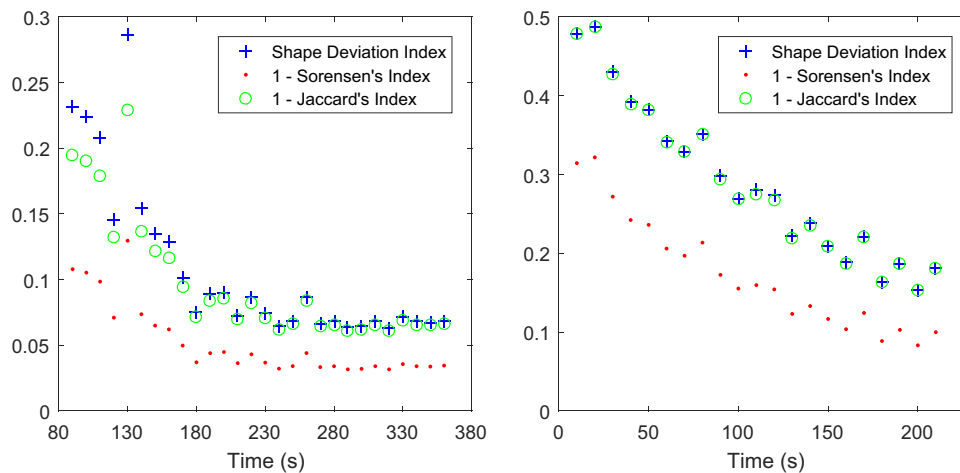


**Fig. 6.** Quantitative evaluation of the perimeter tracking module when applied to the whole footages. Different similarity indices were computed to compare automatic output to manual reference perimeters. Left: Scenario A; right: scenario B.

and forecasts could be expected. Fig. 9 shows the data assimilation process.

In Fig. 9, the matching of modelled and observed isochrones is considerable, which means the data assimilator could successfully capture the observed fire dynamics. Furthermore, flame distortions are present in some remotely sensed isochrones but not in the modelled ones. This fact can be explained because the data assimilation process captures the observed fire behaviour in a way that maximises the system's ability to reproduce the general fire dynamics. Whenever the data assimilation algorithm finds flames, it tends to override them since they constitute unstable phenomena which do not recur always at the same locations. During the assimilation process, the system searched the parametric space composed of the seven fuel and wind parameters until it found their optimum combination. When input to

the propagation model, this combination allowed the obtention of modelled perimeters which resembled the observed. The values used to initialise this optimisation and the validity ranges for all parameters are given in Table 3. Initialisation values were estimated through an educated guess based on the information available in the field. Fig. 10 shows the parameters' convergence towards the minimum of the cost function. Since all these parameters have physical meaning, the validity of the obtained results is easy to assess. In these 2 scenarios, all parameters stayed within their expected range and did not vary significantly from the initial estimated values in general.

Following the assimilation, forecasts were issued for the rest of the recorded sequences making use of the optimised parameters, which are assumed to remain constant for a certain period of time. Fig. 11 summarises the results of this forecast. Again, acceptable rates of

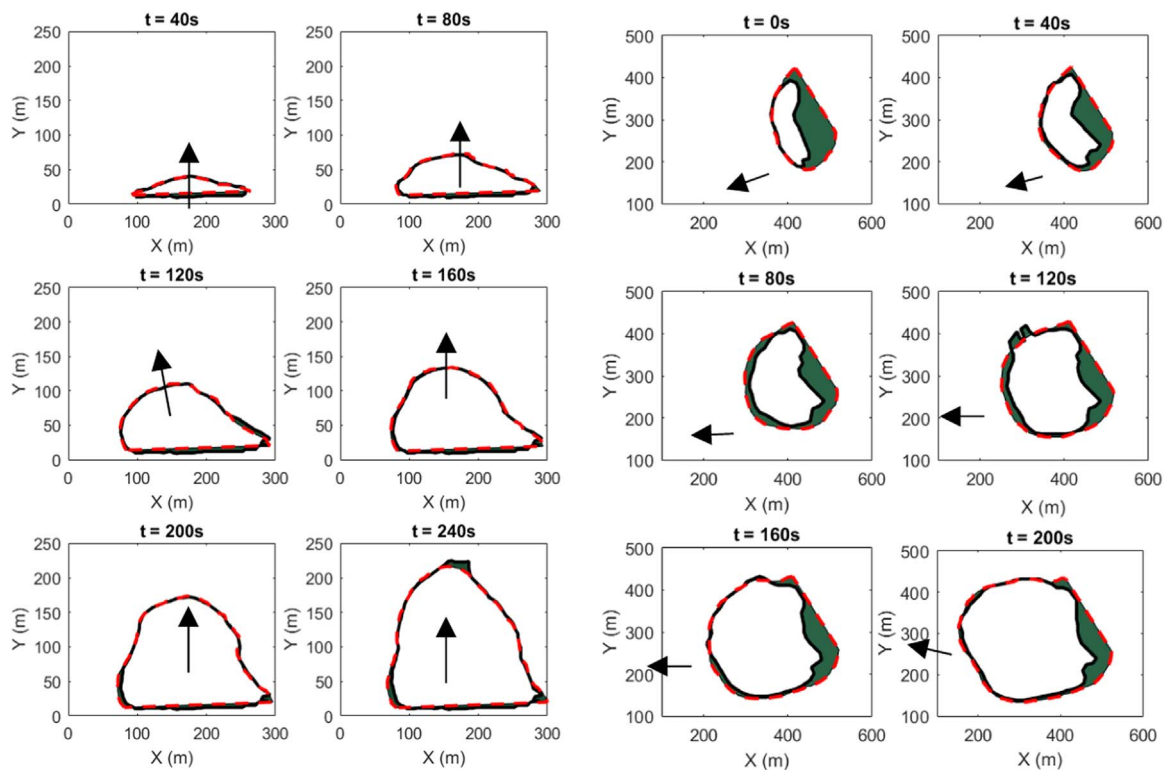


**Fig. 7.** Detailed results of the tracking module for some sample frames. Black solid lines represent detected perimeters and dashed red lines the corresponding manual reference. The error area is shaded in green. Arrows indicate the main propagation direction. Left: Scenario A; right: scenario B. (For interpretation of the references to color in this figure legend, the reader is referred to the web version of this article.)

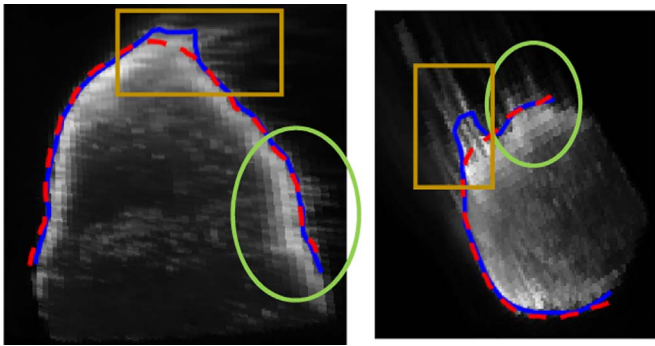


**Fig. 8.** Sample frames affected by flame distortion. Blue solid line: automatic front. Red dashed line: manual reference front. Green ellipses highlight correct flame handling, orange rectangles highlight incorrect behaviour. Left: Scenario A; right: scenario B. (For interpretation of the references to color in this figure legend, the reader is referred to the web version of this article.)

similarity can be observed, which means, on the one hand, that the fire dynamics assimilated from remote sensed perimeters correctly reproduced the actual fire evolution and, on the other, that the forecasting module was able to use those assimilated dynamics to realistically simulate the future perimeter propagation.

For these two scenarios the system needed about 60 s to complete the whole process in a Quad-core Intel i7 personal computer. Obviously, computation times will depend on the computing platform but also on the system configuration itself. There is a significant amount of parameters which can be modified to meet time requirements, e.g. the size of the set of candidates for the Canny hysteresis thresholds, the number of points used to describe perimeters, the tracking frequency and the number of assimilated isochrones. An important fact is that the forecasting stage takes a small percentage of the complete computation, which allows lengthening the emitted forecast without a significant increase in computation time.

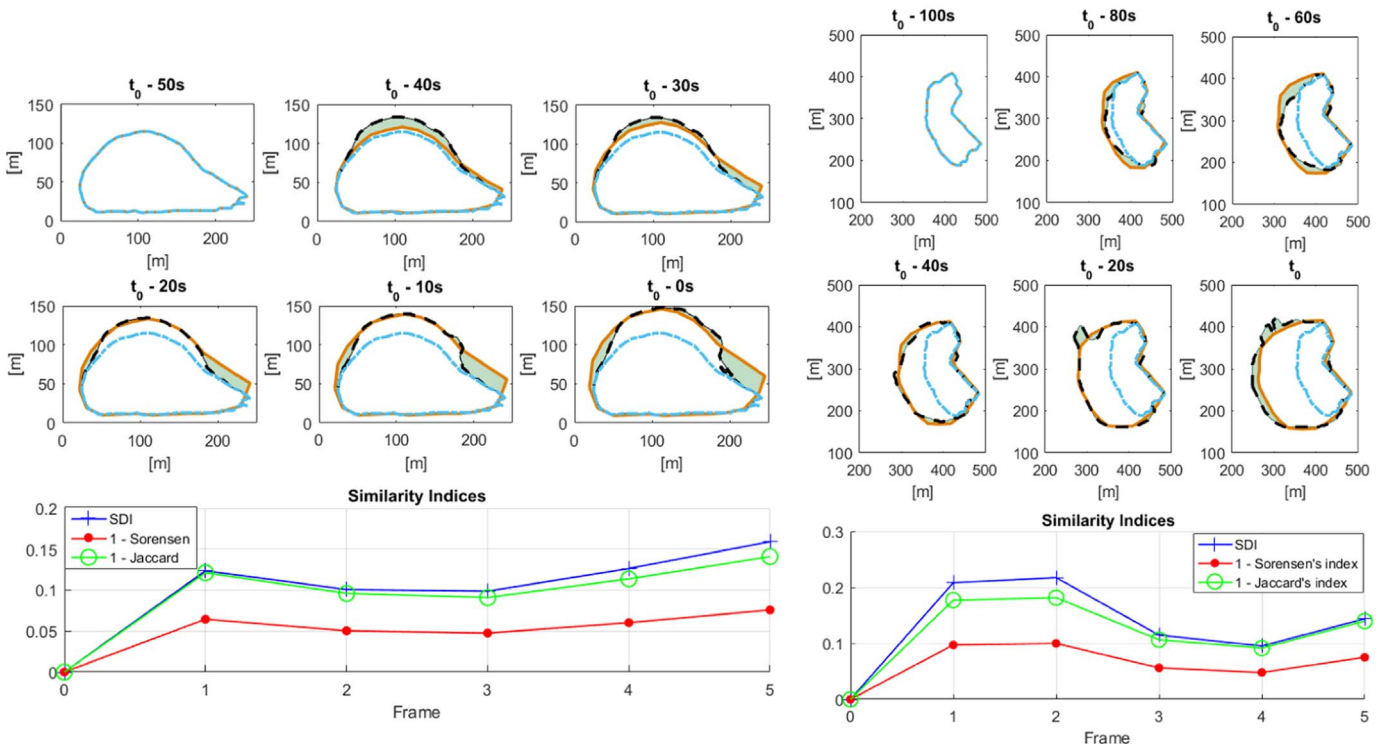


**Fig. 9.** Data assimilation process at time  $t_0$ . Black dashed lines represent the perimeters provided by the tracking module (observed data). Orange solid lines represent the best modelled perimeters which the algorithm could find during the optimisation. The initial perimeter used to launch the propagation model is displayed as a dotted blue line. Error areas are shaded and similarity metrics are included at the bottom. Left: Scenario A; right: scenario B. (For interpretation of the references to color in this figure legend, the reader is referred to the web version of this article.)

**Table 3**

Initialisation values and search spaces for variables assimilated. Validity ranges were extracted from [52].

Variable	Initialisation Value		Range
	Scenario A	Scenario B	
$SAV$	$5000m^{-1}$	$5000m^{-1}$	[3000,11000]
$M_x$	30%	30%	[12,40]
$W_o$	$1kgm^{-2}$	$1kgm^{-2}$	[0.3, 15]
$M_f$	20%	20%	[3,40]
$\delta$	1m	1m	[0.2, 1.9]
$U^0$	$3ms^{-1}$	$3ms^{-1}$	[0,20]
$\theta^0$	0.2rad	4.712rad	[0,2 $\pi$ ]

<sup>a</sup>Fuel model from [52].

## 6. Conclusions and future work

We hereby presented an integral system for the automated tactical monitoring and forecasting of wildland fires. During a wildfire emergency, the amount of accurate real-time information available to emergency responders is usually considerably limited. However, there exist technologies which can contribute to the development of suitable and informative decision support systems. The methodology described in this article proved able to automatically detect the location of the fire perimeter and emit a reliable forecast of its future evolution. It is based on edge detection algorithms applied to TIR aerial imagery and data assimilation techniques, fire rates of spread being computed through an on-line-adjustable Rothermel model. The system was tested in two realistic experimental scenarios with successful results. The remote sensing module was capable of locating the fire perimeter with high accuracy when compared to user manual annotation, the assimilation module correctly captured the remotely sensed fire dynamics and the forecasting module used these assimilated dynamics to forecast the



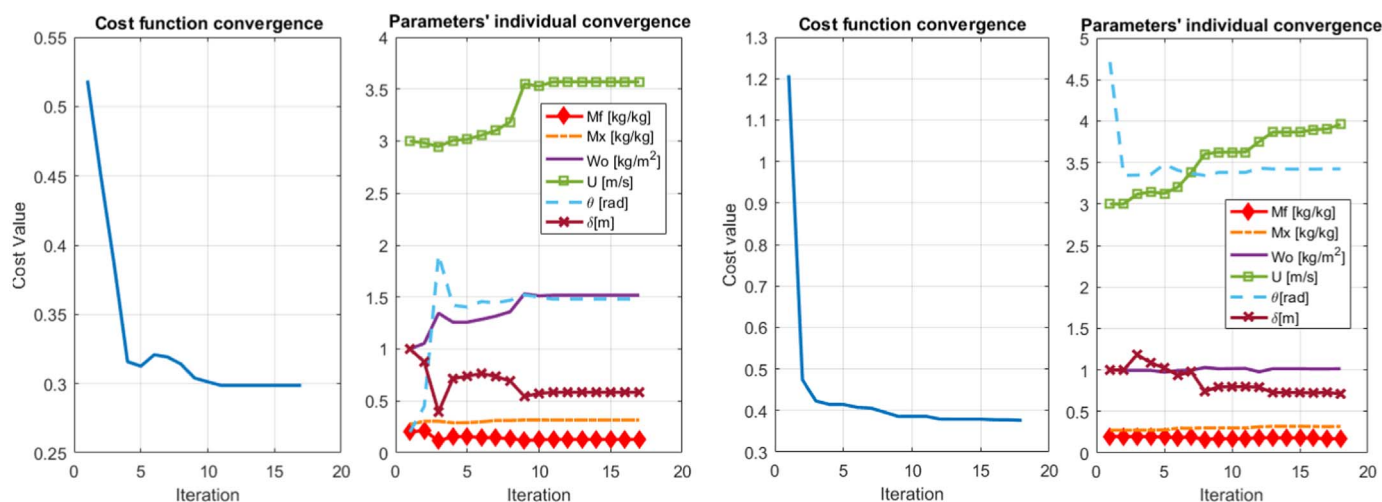


**Fig. 10.** Convergence of optimised parameters towards the minimum of the cost function. Fuel's surface area to volume ratio (SAV) was omitted because it was out of scale. Left: Scenario A; right: scenario B.

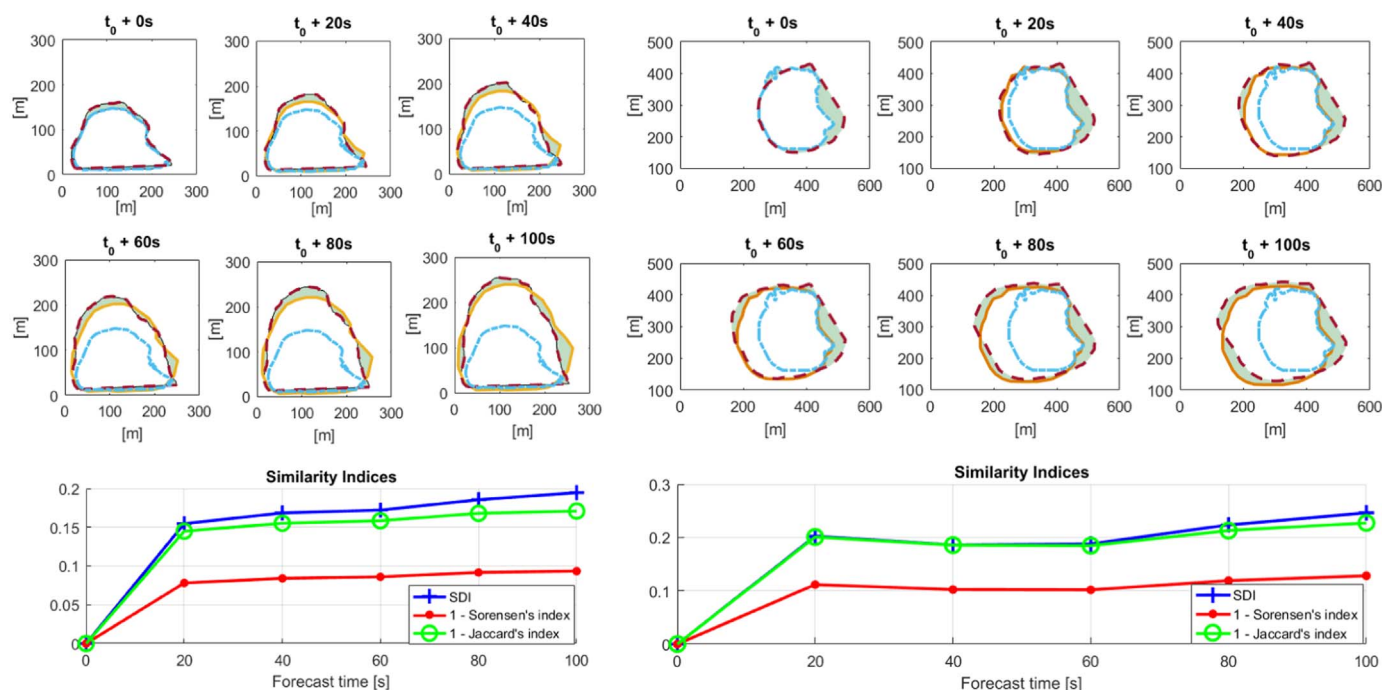


**Fig. 11.** Forecasted fire perimeters (yellow solid lines) assessed by comparison to reference manual isochrones (red dashed lines). The initial perimeter used to launch the propagation model is displayed as a dotted blue line, the error areas are shaded and similarity metrics are included at the bottom. Left: Scenario A; right: scenario B. (For interpretation of the references to color in this figure legend, the reader is referred to the web version of this article.)

upcoming fire evolution. Moreover, the coupling of these three modules helped to overcome a drawback of the perimeter tracker, which was itself unable to filter out flame projections in all cases and occasionally mistook them for the actual fuel burning interface. On the contrary, the overall fire dynamics captured by the assimilation algorithm were not mislead by such flame projections and the consequent forecasted isochrones were not affected by them. Global computation times also proved acceptable for operational scenarios. Therefore, the system is ready to be tested in more complex scenarios with different fuel distributions, different fire regimes and different terrain. If sufficient experimental data becomes available, remotely sensed fire perimeters should be compared to actual on-the-ground measurements. This accuracy information may be used to introduce uncertainty in the data assimilation framework. Finally, in order to become operatively implementable, the surrounding infrastructure should be developed, i.e. a public server should be made available to perform computations

and uplink-downlink communications should be explored so that data can be appropriately delivered to the users in the field.

## Acknowledgements

This research was partially funded by the Spanish Ministry of Economy and Competitiveness (project CTM2014-57448-R, co-financed with FEDER funds), the Spanish Ministry of Education, Culture and Sport (FPU Programme) and the Autonomous Government of Catalonia (project no. 2014-SGR-413). The South Australia experiments were founded by Bushfire Cooperative Research Centre and CSIRO

## References

- [1] J.G. Pausas, Changes in fire and climate in the eastern Iberian Peninsula

- (Mediterranean Basin), *Clim. Change* 63 (2004) 337–350. <http://dx.doi.org/10.1023/b:clim.0000018508.94901.9c>.
- [2] R.A. Shakesby, Post-wildfire soil erosion in the Mediterranean: review and future research directions, *Earth-Sci. Rev.* 105 (2011) 71–100. <http://dx.doi.org/10.1016/j.earscirev.2011.01.001>.
  - [3] M. Flannigan, M. Krawchuk, W. de Groot, B. Wotton, L. Gowman, Implications of changing climate for global wildland fire, *Int. J. Wildl. Fire* 18 (2009) 483–507. <http://dx.doi.org/10.1071/wf08187>.
  - [4] M. Flannigan, A.S. Cantin, W.J. De Groot, M. Wotton, A. Newbery, L.M. Gowman, Global wildland fire season severity in the 21st century, *For. Ecol. Manag.* 294 (2013) 54–61. <http://dx.doi.org/10.1016/j.foreco.2012.10.022>.
  - [5] A. Duane, M. Piqué, M. Castellnou, L. Brotons, Predictive modelling of fire occurrences from different fire spread patterns in Mediterranean landscapes, *Int. J. Wildl. Fire* 24 (2015) 407–418. <http://dx.doi.org/10.1071/wf14040>.
  - [6] M.A. Finney, J.D. Cohen, S.S. McAllister, W.M. Jolly, On the need for a theory of wildland fire spread, *Int. J. Wildl. Fire* 22 (2013) 25–36. <http://dx.doi.org/10.1071/WF11117>.
  - [7] A. González-Cabán, The Economic Dimension of Wildland Fires, in: *Veg. Fires Glob. Chang. Challenges Concert. International Action*, 2013, pp. 229–238.
  - [8] L.B. Lentile, Z.A. Holden, A.M.S. Smith, M.J. Falkowski, A.T. Hudak, P. Morgan, S.A. Lewis, P.E. Gessler, N.C. Benson, Remote sensing techniques to assess active fire characteristics and post-fire effects, *Int. J. Wildl. Fire* 15 (2006) 319. <http://dx.doi.org/10.1071/WF05097>.
  - [9] P.J. Riggan, R.G. Tisell, J.W. Hoffman, Application of the firemapptm thermal-imaging radiometer for wildfire suppression, *IEEE Aerosp. Conf. Proc.* 4 (2003) 1863–1872. <http://dx.doi.org/10.1109/AERO.2003.1235116>.
  - [10] V.G. Ambrosia, S.S. Wegener, Unmanned Airborne Platforms For Disaster Remote Sensing Support, in: *Geosci. Remote Sens.*, 2009. <http://dx.doi.org/10.5772/8302>.
  - [11] V.G. Ambrosia, D.V. Sullivan, S.W. Buechel, Integrating sensor data and geospatial tools to enhance real-time disaster management capabilities: wildfire observations, *Spec. Pap. Geol. Soc. Am.* 482 (2011) 1–12. <http://dx.doi.org/10.1130/9780813724829>.
  - [12] V.G. Ambrosia, S. Wegener, T. Zajkowski, D.V. Sullivan, S. Buechel, F. Enomoto, B. Lobitz, S. Johan, J. Brass, E. Hinkley, The Ikhana unmanned airborne system (UAS) western states fire imaging missions: from concept to reality (2006–2010), *Geocarto Int.* 26 (2011) 85–101. <http://dx.doi.org/10.1080/10106049.2010.539302>.
  - [13] Y. Pérez, E. Pastor, E. Planas, M. Plucinski, J. Gould, Computing forest fires aerial suppression effectiveness by IR monitoring, *Fire Saf. J.* 46 (2011) 2–8. <http://dx.doi.org/10.1016/j.firesaf.2010.06.004>.
  - [14] R. Paugam, M.J. Wooster, G. Roberts, Use of handheld thermal imager data for airborne mapping of fire radiative power and energy and flame front rate of spread, *IEEE Trans. Geosci. Remote Sens.* 51 (2013) 3385–3399. <http://dx.doi.org/10.1109/TGRS.2012.2220368>.
  - [15] D.A. Stow, P.J. Riggan, E.J. Storey, L.L. Coulter, Measuring fire spread rates from repeat pass airborne thermal infrared imagery, *Remote Sens. Lett.* 5 (2014) 803–812. <http://dx.doi.org/10.1080/2150704X.2014.967882>.
  - [16] F. Manzano-Agugliaro, J. Pérez-Aranda, J.L. De La Cruz, Methodology to obtain isochrones from large wildfires, *Int. J. Wildl. Fire* 23 (2014) 338–349. <http://dx.doi.org/10.1071/WF13166>.
  - [17] E. Pastor, L. Zarate, E. Planas, J. Arnaldos, Mathematical models and calculation systems for the study of wildland fire behaviour, *Prog. Energy Combust. Sci.* 29 (2003) 139–153. [http://dx.doi.org/10.1016/S0360-1285\(03\)00017-0](http://dx.doi.org/10.1016/S0360-1285(03)00017-0).
  - [18] A.L. Sullivan, Wildland surface fire spread modelling, 1990–2007. 1: physical and quasi-physical models, *Int. J. Wildl. Fire* 18 (2009) 349–368. <http://dx.doi.org/10.1071/wf06143>.
  - [19] A.L. Sullivan, Wildland surface fire spread modelling, 1990–2007. 2: empirical and quasi-empirical models, *Int. J. Wildl. Fire* 18 (2009) 369–386. <http://dx.doi.org/10.1071/wf06142>.
  - [20] A.L. Sullivan, Wildland surface fire spread modelling, 1990–2007. 3: simulation and mathematical analogue models, *Int. J. Wildl. Fire* 18 (2009) 387–403. <http://dx.doi.org/10.1071/wf06144>.
  - [21] R.R. Linn, A transport model for prediction of wildfire behavior. ([http://www.osti.gov/energycitations/product.biblio.jsp?osti\\_id=505313](http://www.osti.gov/energycitations/product.biblio.jsp?osti_id=505313)), 1997.
  - [22] J.B. Filippi, F. Bosseur, C. Mari, C. Lac, P. Le Moigne, B. Cuenot, D. Veynante, D. Cariolle, J.-H. Balbi, Coupled atmosphere–wildland fire modelling, *J. Adv. Model. Earth Syst.* 2 (2009) 11. <http://dx.doi.org/10.3894/JAMES.2009.1.11>.
  - [23] J.-B. Filippi, F. Bosseur, D. Grandin, FireFire: open-source code for wildland fire spread models, in: *Adv. For. Fire Res.*, 2014: pp. 275–282. [http://dx.doi.org/10.14195/978-989-26-0884-6\\_29](http://dx.doi.org/10.14195/978-989-26-0884-6_29).
  - [24] W. Mell, M.A. Jenkins, J. Gould, P. Cheney, A physics based approach to modeling grassland fires, *Int. J. Wildl. Fire* 16 (2007) 1–22. <http://dx.doi.org/10.1071/wf06002>.
  - [25] D. Viegas, Overview of Forest Fire Propagation Research, in: *Int. Assoc. Fire Saf. Sci. Symp.*, 2011: pp. 95–108. <http://dx.doi.org/10.3801/IAFSS.FSS.10-95>.
  - [26] M.A. Finney, FARSITE: Fire Area Simulator – Model Development and Evaluation. (<http://www.firemodels.org/content/view/full/52/72/>), 1998.
  - [27] K. Tolhurst, B. Shields, D. Chong, Phoenix: development and application of a bushfire risk management tool, *Aust. J. Emerg. Manag.* 23 (2008) 47–54.
  - [28] M.G. Cruz, M.E. Alexander, Uncertainty associated with model predictions of surface and crown fire rates of spread, *Environ. Model. Softw.* 47 (2013) 16–28. <http://dx.doi.org/10.1016/j.envsoft.2013.04.004>.
  - [29] J. Mandel, L.S. Bennethum, J.D. Beezley, J.L. Coen, C.C. Douglas, M. Kim, A. Vodacek, A wildland fire model with data assimilation, *Math. Comput. Simul.* 79 (2008) 584–606. <http://dx.doi.org/10.1016/j.matcom.2008.03.015>.
  - [30] M.C. Rochoux, S. Ricci, D. Lucor, B. Cuenot, A. Trouvé, Towards predictive data-driven simulations of wildfire spread – Part I: reduced-cost ensemble Kalman filter based on a polynomial chaos surrogate model for parameter estimation, *Nat. Hazards Earth Syst. Sci.* 14 (2014) 2951–2973. <http://dx.doi.org/10.5194/nhess-14-2951-2014>.
  - [31] M.C. Rochoux, C. Emery, S. Ricci, B. Cuenot, A. Trouvé, Towards predictive data-driven simulations of wildfire spread – Part II: ensemble Kalman Filter for the state estimation of a front-tracking simulator of wildfire spread, *Nat. Hazards Earth Syst. Sci.* 14 (2015) 2951–2973. <http://dx.doi.org/10.5194/nhess-14-2951-2014>.
  - [32] C. Lautenberger, Wildland fire modeling with an Eulerian level set method and automated calibration, *Fire Saf. J.* 62 (2013) 289–298. <http://dx.doi.org/10.1016/j.firesaf.2013.08.014>.
  - [33] M. Denham, K. Wendt, G. Bianchini, A. Cortés, T. Margalef, Dynamic Data-Driven Genetic Algorithm for forest fire spread prediction, *J. Comput. Sci.* 3 (2012) 398–404. <http://dx.doi.org/10.1016/j.jocs.2012.06.002>.
  - [34] T. Artés, A. Cencerrado, A. Cortés, T. Margalef, D. Rodríguez-Aseretto, T. Petroligakis, J. San-Miguel-Ayaz, Towards a dynamic data driven wildfire behavior prediction system at European level, *Procedia Comput. Sci.* 29 (2014) 1216–1226. <http://dx.doi.org/10.1016/j.procs.2014.05.109>.
  - [35] O. Rios, W. Jahn, G. Rein, Forecasting wind-driven wildfires using an inverse modelling approach, *Nat. Hazards Earth Syst. Sci.* 14 (2014) 1491–1503. <http://dx.doi.org/10.5194/nhess-14-1491-2014>.
  - [36] O. Rios, E. Pastor, M.M. Valero, E. Planas, Short-term fire front spread prediction using inverse modelling and airborne infrared images, *Int. J. Wildl. Fire* 25 (2016) 1033–1047. <http://dx.doi.org/10.1071/WF16031>.
  - [37] M.M. Valero, O. Rios, E. Pastor, E. Planas, Automatic detection of wildfire active fronts from aerial thermal infrared images, in: *Adv. Infrared Technol. Appl.*, Pisa, Italy, 2015.
  - [38] M.M. Valero, O. Rios, E. Pastor, E. Planas, Automated mapping of active wildland fires through aerial infrared imaging and unsupervised edge detection algorithms, *Unpubl. Results.* (n.d.).
  - [39] E.R. Hancock, J. Kittler, Adaptive estimation of hysteresis thresholds, *Proceedings 1991 IEEE Comput. Soc. Conference Comput. Vis. Pattern Recognit* 196–201. <http://dx.doi.org/10.1109/CVPR.1991.139687>, 1991.
  - [40] R. Medina-Carnicer, R. Muñoz-Salinas, E. Yeguas-Bolivar, L. Diaz-Mas, A novel method to look for the hysteresis thresholds for the Canny edge detector, *Pattern Recognit.* 44 (2011) 1201–1211. <http://dx.doi.org/10.1016/j.patcog.2010.12.008>.
  - [41] R.C. Rothermel, A mathematical model for predicting fire spread in wildland fuels, *USDA For. Serv. Res. Pap. INT USA* 40. (<http://www.srs.fs.usda.gov/pubs/32533>), 1972.
  - [42] G.D. Richards, An elliptical growth model of forest fire fronts and its numerical solution, *Int. J. Numer. Methods Eng.* 30 (1990) 1163–1179. <http://dx.doi.org/10.1002/nme.1620300606>.
  - [43] R.H. Byrd, J.C. Gilbert, J. Nocedal, R.H. Byrd, J.C. Gilbert, J. Nocedal, A.T. Region, M. Based, A Trust Region Method Based on Interior Point Techniques for Nonlinear Programming To cite this version: A Trust Region Method Based on Interior Point Techniques for Nonlinear Programming, 185, 2006, pp. 149–185.
  - [44] R.A. Waltz, J.L. Morales, J. Nocedal, D. Orban, An interior algorithm for nonlinear optimization that combines line search and trust region steps, *Math. Program.* 107 (2006) 391–408. <http://dx.doi.org/10.1007/s10107-004-0560-5>.
  - [45] J.B. Filippi, V. Mallet, B. Nader, Evaluation of forest fire models on a large observation database, *Nat. Hazards Earth Syst. Sci.* 14 (2014) 3077–3091. <http://dx.doi.org/10.5194/nhess-14-3077-2014>.
  - [46] W. Cui, A.H. Perera, Quantifying spatio-temporal errors in forest fire spread modelling explicitly, *J. Environ. Inform.* 16 (2010) 19–26. <http://dx.doi.org/10.3808/jei.201000174>.
  - [47] T. Sorensen, A method of establishing groups of equal amplitude in plant sociology based on similarity of species and its application to analyses of the vegetation on Danish commons, *Biol. Skr.* 5 (1948) 1–34.
  - [48] P. Jaccard, Étude comparative de la distribution florale dans une portion des Alpes et du Jura, *Bull. La Société Vaud. Des. Sci. Nat.* 37 (1901) 547–579.
  - [49] M.G. Cruz, S. Matthews, J. Gould, P. Ellis, Fire dynamics in mallee-heath: fuel, weather and fire behaviour prediction in south Australian semi-arid shrublands, *Bushfire Coop. Res. Cent. Tech. Rep.* A 10.01 (2010) (<http://www.bushfirecrcc.com/sites/default/files/firedynamicsinmalleeheathreport.pdf>).
  - [50] M. Plucinski, E. Pastor, Criteria and methodology for evaluating aerial wildfire suppression, *Int. J. Wildl. Fire* 22 (2013) 1144–1154. <http://dx.doi.org/10.1071/WF13040>.
  - [51] E. Pastor, A. Àgueda, J. Andrade-Cetto, M. Muñoz, Y. Pérez, E. Planas, Computing the rate of spread of linear flame fronts by thermal image processing, *Fire Saf. J.* 41 (2006) 569–579. <http://dx.doi.org/10.1016/j.firesaf.2006.05.009>.
  - [52] J.H. Scott, R.E. Burgan, Standard fire behavior fuel models: a comprehensive set for use with Rothermel's surface fire spread model, *Bark. Beetles Fuels Fire Bibliogr.* (2005) 66.